

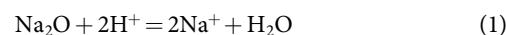
Implications for metal and volatile cycles from the pH of subduction zone fluids

Matthieu E. Galvez¹, James A. D. Connolly¹ & Craig E. Manning²

The chemistry of aqueous fluids controls the transport and exchange—the cycles—of metals^{1–5} and volatile elements^{3,6,7} on Earth. Subduction zones, where oceanic plates sink into the Earth's interior, are the most important geodynamic setting for this fluid-mediated chemical exchange^{2,6–10}. Characterizing the ionic speciation and pH of fluids equilibrated with rocks at subduction zone conditions has long been a major challenge in Earth science^{11,12}. Here we report thermodynamic predictions of fluid–rock equilibria that tie together models of the thermal structure, mineralogy and fluid speciation of subduction zones. We find that the pH of fluids in subducted crustal lithologies is confined to a mildly alkaline range, modulated by rock volatile and chlorine contents. Cold subduction typical of the Phanerozoic eon¹³ favours the preservation of oxidized carbon in subducting slabs. In contrast, the pH of mantle wedge fluids is very sensitive to minor variations in rock composition. These variations may be caused by intramantle differentiation, or by infiltration of fluids enriched in alkali components extracted from the subducted crust. The sensitivity of pH to soluble elements in low abundance in the host rocks, such as carbon, alkali metals and halogens, illustrates a feedback between the chemistry of the Earth's atmosphere–ocean system^{14,15} and the speciation of subduction zone fluids via the composition of the seawater-altered oceanic lithosphere. Our findings provide a perspective on the controlling reactions that have coupled metal and volatile cycles in subduction zones for more than 3 billion years⁷.

Water-based chemical reactions are essential to Earth's surface chemistry. Water is also crucial to our planet's inner chemical dynamics. Subduction zones are the primary locations where surface water is delivered to the deep Earth, promoting low-temperature (T) melting of the crust¹⁶ and mantle⁹, affecting the rheology of the lithosphere¹⁷, blurring pre-metamorphic signatures of ancient Earth's palaeo-environmental conditions^{10,18} and contributing to the global recycling of volatiles^{6–8} and metals^{2,6,8}. Consequently, characterizing the reactivity of supercritical aqueous solutions in subduction zones is a problem of both scientific and societal relevance in Earth science. The key variables that control rock mineralogy and fluid chemistry are pressure (P), T and composition, which in combination govern, for example, fluid redox state⁶, speciation⁵ and electrical properties¹¹. Although the redox budget of subduction zones has been the subject of growing attention⁶, obtaining quantitative constraints on their acid–base budget and on the ionic (for example, the pH; refs 5, 12) and molecular composition of fluids at mantle conditions has proven difficult in both theory and experiment^{11,12}. Recent molecular dynamic simulations have extended the range of conditions at which the solvent property of water (its dielectric constant ϵ_r , Extended Data Fig. 1) is known to upper-mantle conditions^{19,20}, and these results have been generalized for geologically ubiquitous carbonic fluids^{21,22}. However, geochemical applications remain hindered by insufficient knowledge about the sensitivity of fluid properties to changing mineralogical assemblages at the elevated P and T prevalent in the Earth's interior.

We address this problem using a thermodynamic approach²² that connects fluid composition and speciation to predicted rock mineralogy as a function of P and T . After determining the P – T stability fields of solid–solvent phase assemblages for crustal and mantle lithologies (Fig. 1, Methods and Extended Data Table 1), the chemical potentials from the mineralogical model are used to derive fluid speciation (Figs 2 and 3) using oxide hydrolysis equilibria represented, for example, by the alkali – proton exchange reaction:



We assume fluid–rock equilibrium holds at all conditions, as supported by rapid rates of mineral dissolution and precipitation in hydrothermal fluids²³; our results hold for common scenarios of pervasive fluid flow at low transport rates where grain boundary diffusion dominates. Redox reactions of Fe have been discounted, that is, the redox composition of the fluid (O/H ratio) is determined by the devolatilization process. At equilibrium, under the assumption of rock-dominated chemistry, the chemical potential (μ) of oxides constrains fluid speciation by:

$$\underbrace{\mu_{\text{Na}_2\text{O}} - \mu_{\text{H}_2\text{O}}}_{\text{mineralogical model}} = 2 \underbrace{(\mu_{\text{Na}^+} - \mu_{\text{H}^+})}_{\text{solute speciation}} \quad (2)$$

The partial molar Gibbs energy of the i th solute is $\mu_i = g_i^\ominus + RT \ln(\gamma_i m_i)$, where g_i^\ominus is the standard-state Gibbs energy of 1 mol of solute per kg of solvent at P and T . Here γ_i is the solute activity coefficient, m_i the molal concentration, their product $\gamma_i m_i$ is the activity (a) of i , and $\text{pH} = -\log_{10}(a_{\text{H}^+})$. Thermochemical data for minerals, solvents and solutes are reported in Methods and Extended Data Table 2. This approach provides fluid speciation and pH by charge balance (Methods), and is original in that it tracks the release of all soluble elements simultaneously. We focus on pH, and particular emphasis is placed on testing the sensitivity of predictions to change in P – T conditions and rock composition (Figs 2 and 3).

The fluid alkalinity is defined by $\Delta\text{pH} = \text{pH} - \text{pH}_n$, which tracks the acidic ($\Delta\text{pH} < 0$) or alkaline ($\Delta\text{pH} > 0$) character of the fluid with respect to acid–base neutrality. Neutral pH ($\text{pH}_n = 0.5[\text{p}K_w - \log_{10}(a_{\text{H}_2\text{O}})]$) is defined as the condition where $a_{\text{H}^+} = a_{\text{OH}^-}$, and, accordingly, model ΔpH takes into account the modification of water activity and ionization constant (K_w) in the mixed solvents. Crustal pelite and basalt exhibit similar isothermal trends of ΔpH when H_2O is the solvent. This pattern reflects uniform variations in partial molar volume of Na_2O in these systems where sodic phases include feldspar (albite, Ab), mica (paragonite, Par), clinopyroxene (jadeite, Jd) and amphibole (Fig. 1a, b). The ΔpH reaches a maximum at conditions corresponding to the $\text{Ab} = \text{Jd} + \text{Quartz (Q)}$ reaction, and is in the range 2.3 ± 0.2 along representative cold and intermediate P – T paths (Figs 1, 2d). The ΔpH of fluids equilibrated with an alkali-free mantle peridotite spans a larger range. It peaks near 2.1 ± 0.2 , reflecting incompatible behaviour of calcium in the ultramafic system, at 400–500 °C,

¹Earth Sciences Department, Swiss Federal Institute of Technology, CH-8092 Zurich, Switzerland. ²Department of Earth, Planetary and Space Sciences, University of California, Los Angeles, California 90095-1567, USA.

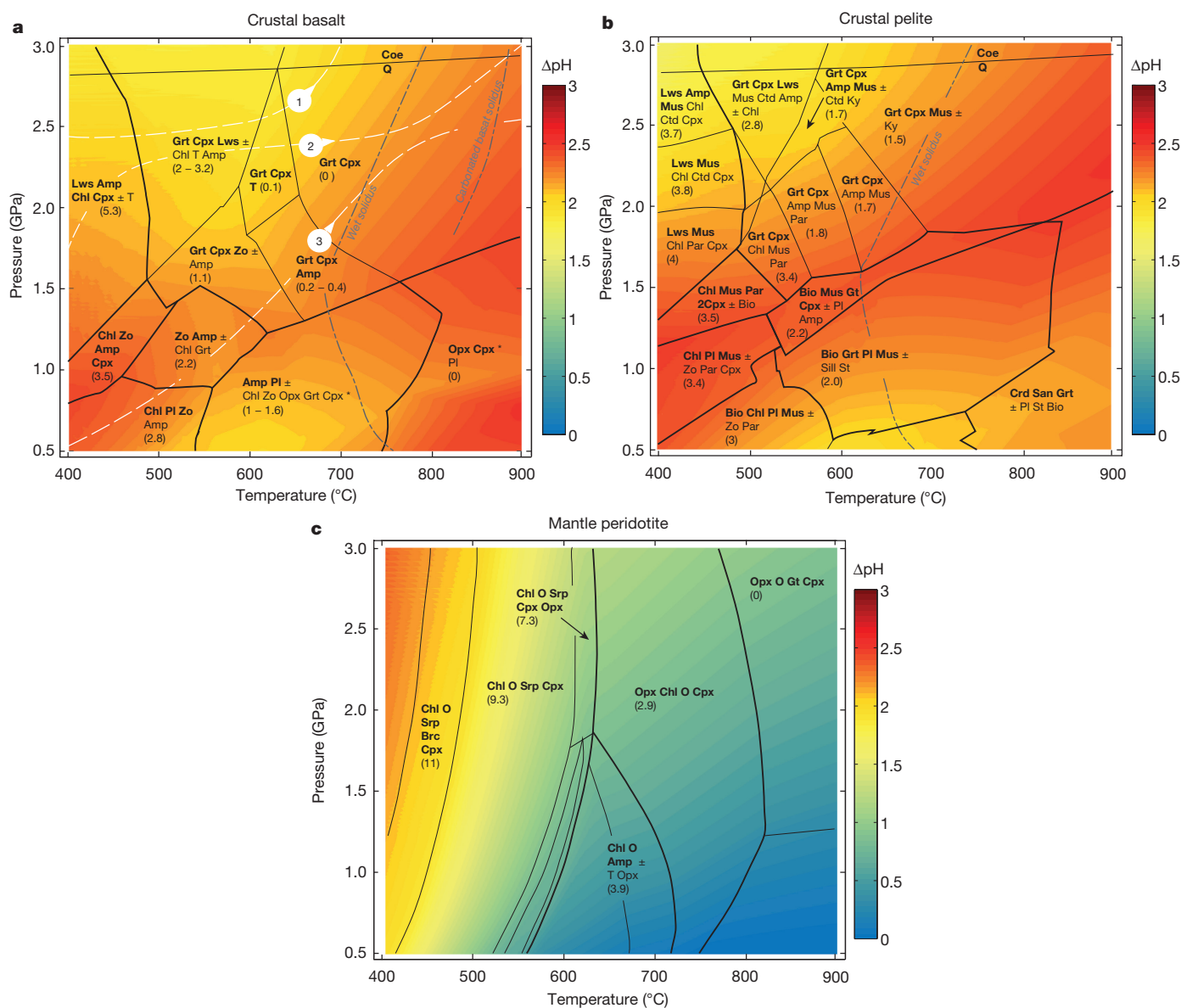


Figure 1 | ΔpH of solutions in equilibrium with basalt, pelite and peridotite lithologies. Here $\Delta\text{pH} = \text{pH} - \text{pH}_n$ describes the deviation of fluid pH from pH at acid–base neutrality, pH_n (see text and Methods). It is plotted against the stable mineral assemblages (that label each field) as a function of P and T for basalt (a), pelite (b) and peridotite (alkali-free lherzolite) (c) compositions (Extended Data Table 1) at equilibrium with H_2O . Mineral abbreviations (defined in Methods) in bold denote phases present in the entire field, those in plain text appear in some parts of the field. Indicative amounts of H_2O structurally bound in minerals are given in parentheses in wt% below the characteristic phase assemblage. Decreasing amount of H_2O in the mineral assemblage with heating indicates progressive rock dehydration. The carbonated basalt (Fig. 2)

and declines to about 1.0 with heating and transition to chlorite- and garnet-peridotite along cold and intermediate P - T paths (Figs 1c, 2d). These trends are maintained along the path representative of hot Precambrian subduction zones¹³ (Figs 1a, 2a).

Carbonic solvents formed if graphite or carbonate are present in the pelite (redox neutral solvent with atomic ratio $\text{O}/\text{H} = 1/2$) and basalt (oxidized, $\text{O}/\text{H} > 1/2$), respectively, are characterized by lower H_2O activity ($0.6 \leq a_{\text{H}_2\text{O}} < 1$). The ΔpH of the C-bearing solutions decreases by up to 0.7 units for the carbonated-basalt fluids (Fig. 2b, e). Their carbon abundance (Fig. 3a) is about one order of magnitude greater than in fluids equilibrated with graphitic pelite¹⁰. Although metal solubilities are semiquantitative at these conditions^{21,24}, the $(\text{Na} + \text{K})/\text{Al}$

differs from the C-free system by the presence of calcite/aragonite (up to ~ 1.3 GPa), dolomite (~ 1 – 1.9 GPa) and magnesite above ~ 1.9 GPa. Two Phanerozoic P - T paths (white dashed lines), that is, Honshu ('cold' path, labelled 1) and Columbia ('intermediate' path, 2) are indicated in a along with a 'hot' P - T path (path 3) (Methods). Dash-dotted curves in grey are approximate experimental locations of the wet basalt/pelite solidii in a and b, and also show the carbonated-basalt solidus in a (Methods). All fields for basalt and pelite, with the exception of those marked with an asterisk where quartz is not stable at $P < 0.7$ GPa and $T > 600$ °C, contain quartz or coesite (Coe). Thick lines designate boundaries between classical metamorphic facies referred to in Fig. 2. Precision on absolute ΔpH values is ± 0.2 ΔpH . Accuracy is within 1 ΔpH unit (Methods).

ratios of fluids increases, by a factor of 2 to 20 for pelite and basalt, respectively, with minor bulk-rock solubility increase. These modifications are due to competing solvent (H_2O dilution with non-dipolar molecules such as CO_2 and CH_4), pH (carbonate equilibria and equation (2)), and speciation effects (alkali-carbonate ion pairing). It illustrates that the ability of subduction zone fluids to dissolve metals, irrespective of their accessible oxidation state, depends on the fluid's volatile speciation, and thus redox state. Similarly, the solubility of C and the C/Ca ratio in the basaltic fluid increase with heating and decompression (Fig. 3a, b). These trends are supported by experimental evidence²⁵, and controlled by incongruent dissolution of Ca-Mg-Fe carbonate. Along hot to intermediate geotherms, crustal and oceanic

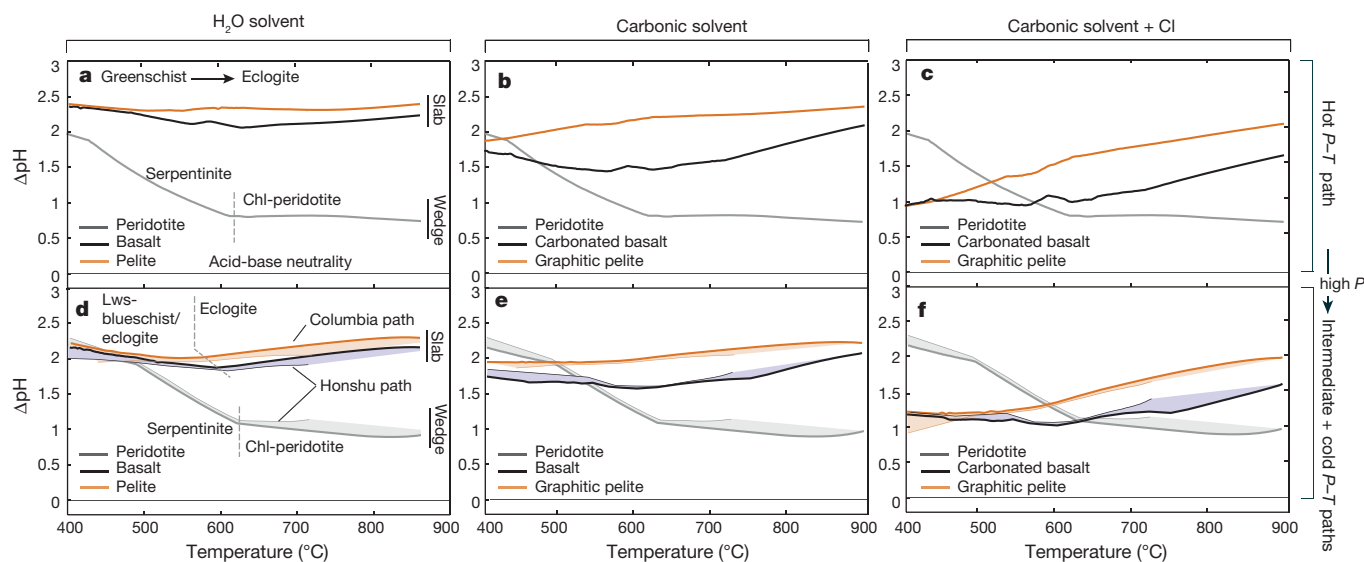


Figure 2 | ΔpH along three representative Precambrian and Phanerozoic P - T paths. The three paths are shown in Fig. 1a. **a–f**, ΔpH of a pure H_2O solvent (**a**, **d**) at equilibrium with peridotite (grey), basalt (red) and pelite (yellow) along hot (**a–c**), intermediate and cold P - T paths (**d–f**) (see Methods for details). **b**, **e**, Results obtained for a carbonic solvent, that is, with C added to the pelite (redox-neutral solvent, $a_{\text{C}} = 1$, $\text{O}/\text{H} = 0.5$ (atomic ratio) and $a_{\text{CO}_2} \approx a_{\text{CH}_4}$) and basalt (H_2O - CO_2 solvent, $\text{O}/\text{H} > 0.5$). Greater C solubility and CO_2 ionization (carbon species include, CaHCO_3^+ , CaCO_3^0 , HCO_3^- , NaCO_3^- , CO_3^{2-}

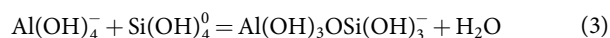
$\pm \text{HCOO}^-$, Extended Data Table 2) account for larger ΔpH drop in the carbonated basalt compared to the graphite-bearing pelite system. **c**, **f**, Results obtained for carbonic solvents including 1 molal total chlorine (Methods). The effect of chlorine is most pronounced at low- T conditions where it is fully ionized, and its abundance in the fluid exceeds the ionic strength of Cl-free solutions, $I \approx 0.1$, by ~ 1 order of magnitude. Major metamorphic facies transitions are indicated in **a**, **d**, and acid-base neutrality ($\Delta\text{pH} = 0$) is indicated by the horizontal baseline in each panel. The P - T paths refer to those defined in Fig. 1.

mantle dehydration occur at shallow depths (< 3 GPa ≈ 80 km, Fig. 1) and are concomitant with elevated C solubility (4–10 mol C per kg H_2O , Fig. 3b), favouring ample fore-arc carbonate dissolution and melting (Methods, Extended Data Table 3). This regime characterizes hot Precambrian subduction zones and rare modern equivalents. The cold path differs fundamentally in that slab dehydration is limited, and confined to elevated P (Fig. 1a) and low T where the solubility of carbon is relatively low (0.3–3 mol per kg H_2O ; Fig. 3a). Thus, cold paths typical of the Phanerozoic favour the mechanical incorporation of carbonates in the deep upper mantle (Methods, Extended Data Table 3), in agreement, for example, with the ubiquitous persistence of Ca-Mg-Fe carbonates in ultra-high- P terranes on Earth²⁶. This temporal directionality implies that the return of surface O to the mantle by slab carbonates is enhanced by subduction cooling over geological time (Extended Data Table 3). The formation of extensive domains of mantle redox heterogeneities, and their associated processes^{10,27}, may be a geologically recent phenomenon.

Addition of chlorine in amounts typical of dilute subduction zone fluids²⁸ shifts predicted ΔpH closer to neutrality regardless of thermal structure (Fig. 2c, f). Thus, at $T > 500$ °C, the ΔpH of the three studied lithologies is confined to a narrow mildly alkaline range (Fig. 2). Larger contrasts develop at lower temperatures, or at elevated T and P lower than 1 GPa (Fig. 1) characterized by enhanced ion association and complex neutralization, and, thus, pH is a less pertinent system variable. The ΔpH is particularly sensitive to seawater components in the altered oceanic lithosphere such as carbon, alkali and halogen (Fig. 2). Slab thermal structure plays a subordinate role in determining pH, but exerts an important control on the geochemical systematics of the volatile-rich fluids (Fig. 3a, b).

These findings are also illustrated by the evolution of fluid chemistry across a chemical profile ranging from an alkali-depleted mantle composition to a model slab fluid composition (component \mathcal{F} in Fig. 3c, d and Extended Data Table 1). This scenario tests the role of chemical variability, introduced by metasomatism or intramantle differentiation, on fluid chemistry. At 600 °C, 2 GPa and minor rock Na_2O content ($w_{\text{Na}_2\text{O}}^{\text{rock}}$) of 0–0.1 wt% (in clinopyroxene), that is, alkali

compositions typical of depleted supra-subduction-zone mantle peridotite²⁹, the pronounced increase of $\mu_{\text{Na}_2\text{O}}$ (Extended Data Fig. 2) is not fully accommodated by enhanced deprotonation of, for example, $\text{Si}(\text{OH})_4^0$ to $\text{Si}(\text{OH})_3^-$ (Extended Data Fig. 3) and leads to a residual ΔpH increase exceeding 2 log units (Fig. 3c, d). The variations deviate significantly from a linear mixing trend between endmember fluid compositions, and highlight the limited acid–base buffering capacity of ubiquitous ultramafic mineral assemblages characterized by low alkali concentrations. Previous models of nitrogen speciation in the mantle³⁰ may be revised in light of these new constraints. The formation of Na,K-bearing assemblages including clinopyroxene, biotite and amphibole stabilizes ΔpH at strongly alkaline values (as previously anticipated by ref. 31)— $\Delta\text{pH} \geq 3$ –4 over the interval 400–900 °C at 2 GPa; pH values then gently decline along a sub-linear mixing trend with further addition of component \mathcal{F} . Low values of μ_{SiO_2} in mantle peridotites (Extended Data Fig. 2) would act as a geochemical trap for a range of silica-bearing polynuclear clusters that carry trace elements in metasomatic fluids derived from the slabs^{24,32} (Extended Data Fig. 3). The formation of mica (at $X_{\mathcal{F}} = 0.43$, Fig. 3d) causes a drop of ΔpH , and a coincident increase of μ_{SiO_2} , $\mu_{\text{Al}_2\text{O}_3}$ (Extended Data Fig. 2). These conditions would promote the high- T formation of silica–aluminate complexes³³, not considered here for lack of relevant thermochemical data, by condensation reactions such as:



We anticipate that the formation of these solutes would increase the solubility of cations (as required from electroneutrality) and bring ΔpH values closer to acid–base neutrality. Further work is needed to quantify the efficiency of this mechanism. Experimental strategies for pH and electrical transport¹¹ measurements in high- P fluids are required.

Taken together, our results show that acid–base mechanisms important for the dissolution, transport and deposition of metals, for example pH fluctuations, are not restricted to upper-crustal magmatic–hydrothermal environments^{4,5}—they are significant in

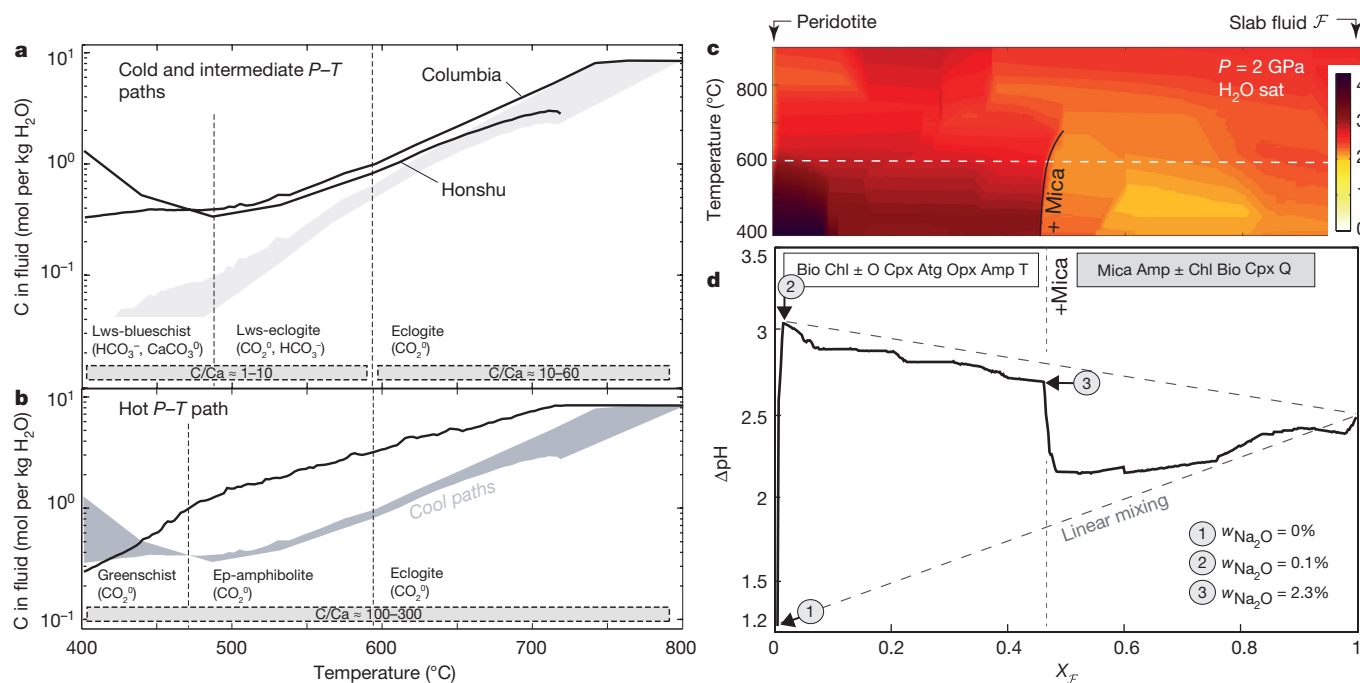


Figure 3 | Metasomatism at the subduction interface. **a**, C content of a fluid at equilibrium with carbonated basalt along cold and intermediate P - T paths. **b**, C content of the fluid along the hot P - T path. C abundance is displayed here in moles of C per kg of H_2O . Atomic ratio C/Ca along those paths is indicated. It is particularly sensitive to the P - T conditions, rising very rapidly to above 10^3 with heating and decompression. Enhancement of C solubility with pressure, a peculiar feature confined to $P > 2$ -2.5 GPa and $T < 500$ °C (The stable carbonate phase is Fe-Mg carbonate 'Magnesite'), is due to extensive Ca-carbonate complexing in the fluid. Predictions from simple molecular fluid models are indicated along the same paths (pale grey area, **a**). Discrepancies between the models are as expected largest at low T and elevated P . Vertical dashed lines indicate

polar solvents present at the slab interface. Factors controlling these fluctuations include (1) mineralogical heterogeneities, (2) the presence of minor but soluble components in solid solutions, (3) variations of the activity and structure of H_2O in mixed-volatile solvents, and (4) the speciation of coordinating ligands. In particular, sulfur may form abundant dipolar H_2S and SO_2 molecules and various ligands, the distribution of which is redox and pH sensitive³ and will influence the transport of metals such as Au and Cu along the subduction interface. Our work places quantitative pH restrictions on the identity and solubility of aqueous metal-complexes pertinent to these processes. The development and generalization of acid-base formalisms to coexisting rock-fluid-melt systems will be necessary at T greater than 750–800 °C (Fig. 1a, Methods).

The present work focused on fundamental chemical characteristics of aqueous fluids at upper-mantle conditions, which improves our ability to interpret compositional variability in rocks exhumed from the Earth's interior^{18,21}. Metal-volatile chemical coupling is a consequence of mineralogical equilibria and electrostatic interactions in fluids. Their nonlinear behaviour and mildly alkaline nature reflect intrinsic properties of silicate mineralogies. The sensitivity of fluid pH to soluble elements in low abundance in the host rock, such as carbon, alkali and halogens, illustrates a feedback between the chemistry of the Earth's atmosphere-ocean system^{7,14} and the behavior of metals and volatiles in subduction zones via the composition of the seawater-altered oceanic lithosphere¹⁵. Our results also permit quantification of the electrical conductivity of subduction zone fluids¹¹.

Online Content Methods, along with any additional Extended Data display items and Source Data, are available in the online version of the paper; references unique to these sections appear only in the online paper.

boundaries of metamorphic facies (for example, lawsonite (Lws)-eclogite), and indications on C speciation (for example CO_2 , HCO_3^-). **c**, Variations of ΔpH (colour coded) for $T = 400$ – 900 °C and $P = 2$ GPa obtained by mixing peridotite composition with model metasomatic component $\mathcal{F} = Na(K,Ca,Mg,Fe)_{1/3}Al_{1.5}Si_{17.9}O_{17.9}$ (expressed in mole fraction of the ultramafic- \mathcal{F} oxide mixture, $X_{\mathcal{F}}$) at H_2O saturation (H_2O sat.). Thick black line indicates appearance of white mica (+ Mica) in the assemblage. **d**, Section plot of **c** at 600 °C with indications of mineral assemblages and corresponding values of Na_2O abundance in the rock (arrows, $w_{Na_2O}^{rock}$ in wt%). Dashed grey lines indicate linear mixing between endmember fluid compositions.

Received 11 December 2015; accepted 14 September 2016.

- Eugster, H. P. Minerals in hot water. *Am. Mineral.* **71**, 655–673 (1986).
- Hedenquist, J. W. & Lowenstern, J. B. The role of magmas in the formation of hydrothermal ore deposits. *Nature* **370**, 519–527 (1994).
- Pokrovski, G. S. & Dubrovinsky, L. S. The S_3^- ion is stable in geological fluids at elevated temperatures and pressures. *Science* **331**, 1052–1054 (2011).
- Phillips, G. N. & Evans, K. A. Role of CO_2 in the formation of gold deposits. *Nature* **429**, 860–863 (2004).
- Dolejs, D. & Wagner, T. Thermodynamic modeling of non-ideal mineral-fluid equilibria in the system Si-Al-Fe-Mg-Ca-Na-K-H-O-Cl at elevated temperatures and pressures: implications for hydrothermal mass transfer in granitic rocks. *Geochim. Cosmochim. Acta* **72**, 526–553 (2008).
- Evans, K. A. The redox budget of subduction zones. *Earth Sci. Rev.* **113**, 11–32 (2012).
- Hayes, J. M. & Waldbauer, J. R. The carbon cycle and associated redox processes through time. *Phil. Trans. R. Soc. Lond. B* **361**, 931–950 (2006).
- Eiler, J. M., McInnes, B., Valley, J. W., Graham, C. M. & Stolper, E. M. Oxygen isotope evidence for slab-derived fluids in the sub-arc mantle. *Nature* **393**, 777–781 (1998).
- Stolper, E. & Newman, S. The role of water in the petrogenesis of Mariana trough magmas. *Earth Planet. Sci. Lett.* **121**, 293–325 (1994).
- Galvez, M. E. *et al.* Graphite formation by carbonate reduction during subduction. *Nat. Geosci.* **6**, 473–477 (2013).
- Ni, H., Chen, Q. & Keppler, H. Electrical conductivity measurements of aqueous fluids under pressure with a hydrothermal diamond anvil cell. *Rev. Sci. Instrum.* **85**, 115107 (2014).
- Ding, K. & Seyfried, W. E. Direct pH measurement of NaCl-bearing fluid with an in situ sensor at 400 °C and 40 megapascals. *Science* **272**, 1634–1636 (1996).
- Brown, M. Duality of thermal regimes is the distinctive characteristic of plate tectonics since the Neoproterozoic. *Geology* **34**, 961–964 (2006).
- Anbar, A. D. Elements and evolution *Science* **322**, 1481–1483 (2008).
- Staudigel, H. & Hart, S. R. Alteration of basaltic glass: Mechanisms and significance for the oceanic crust-seawater budget. *Geochim. Cosmochim. Acta* **47**, 337–350 (1983).

16. Poli, S. Carbon mobilized at shallow depths in subduction zones by carbonatitic liquids. *Nat. Geosci.* **8**, 633–636 (2015).
17. Hirth, G. & Kohlstedt, D. L. Water in the oceanic upper mantle: implications for rheology, melt extraction and the evolution of the lithosphere. *Earth Planet. Sci. Lett.* **144**, 93–108 (1996).
18. Fischer, W. W. *et al.* SQUID–SIMS is a useful approach to uncover primary signals in the Archean sulfur cycle. *Proc. Natl Acad. Sci. USA* **111**, 5468–5473 (2014).
19. Pan, D., Spanu, L., Harrison, B., Sverjensky, D. A. & Galli, G. Dielectric properties of water under extreme conditions and transport of carbonates in the deep Earth. *Proc. Natl Acad. Sci. USA* **110**, 6646–6650 (2013).
20. Sverjensky, D. A., Harrison, B. & Azzolini, D. Water in the deep Earth: the dielectric constant and the solubilities of quartz and corundum to 60kb and 1200° C. *Geochim. Cosmochim. Acta* **129**, 125–145 (2014).
21. Galvez, M. E., Manning, C. E., Connolly, J. A. & Rumble, D. The solubility of rocks in metamorphic fluids: a model for rock-dominated conditions to upper mantle pressure and temperature. *Earth Planet. Sci. Lett.* **430**, 486–498 (2015).
22. Mountain, R. D. & Harvey, A. H. Molecular dynamics evaluation of dielectric constant mixing rules for H₂O–CO₂ at geologic conditions. *J. Solution Chem.* **44**, 2179–2193 (2015).
23. Wood, B. J. & Walther, J. V. Rates of hydrothermal reactions. *Science* **222**, 413–415 (1983).
24. Manning, C. E., Antignano, A. & Lin, H. A. Premelting polymerization of crustal and mantle fluids, as indicated by the solubility of albite + paragonite + quartz in H₂O at 1GPa and 350–620° C. *Earth Planet. Sci. Lett.* **292**, 325–336 (2010).
25. Aranovich, L. Y. & Newton, R. C. Experimental determination of CO₂–H₂O activity-composition relations at 600–1000 degrees C and 6–14 kbar by reversed decarbonation and dehydration reactions. *Am. Mineral.* **84**, 1319–1332 (1999).
26. Liou, J., Zhang, R. & Ernst, W. Occurrences of hydrous and carbonate phases in ultrahigh-pressure rocks from east-central China: implications for the role of volatiles deep in cold subduction zones. *Isl. Arc* **4**, 362–375 (1995).
27. Rohrbach, A. & Schmidt, M. W. Redox freezing and melting in the Earth's deep mantle resulting from carbon-iron redox coupling. *Nature* **472**, 209–212 (2011).
28. Li, H. & Hermann, J. Apatite as an indicator of fluid salinity: an experimental study of chlorine and fluorine partitioning in subducted sediments. *Geochim. Cosmochim. Acta* **166**, 267–297 (2015).
29. Parkinson, I. J. & Pearce, J. A. Peridotites from the Izu–Bonin–Mariana forearc (ODP Leg 125): evidence for mantle melting and melt–mantle interaction in a supra-subduction zone setting. *J. Petrol.* **39**, 1577–1618 (1998).
30. Mikhail, S. & Sverjensky, D. A. Nitrogen speciation in upper mantle fluids and the origin of Earth's nitrogen-rich atmosphere. *Nat. Geosci.* **7**, 816–819 (2014).
31. Ryabchikov, I., Schreyer, W. & Abraham, K. Compositions of aqueous fluids in equilibrium with pyroxenes and olivines at mantle pressures and temperatures. *Contrib. Mineral. Petrol.* **79**, 80–84 (1982).
32. Wilke, M. *et al.* Zircon solubility and zirconium complexation in H₂O+Na₂O+SiO₂+Al₂O₃ fluids at high pressure and temperature. *Earth Planet. Sci. Lett.* **349–350**, 15–25 (2012).
33. Salvi, S., Pokrovski, G. S. & Schott, J. Experimental investigation of aluminum-silica aqueous complexing at 300 C. *Chem. Geol.* **151**, 51–67 (1998).

Acknowledgements The presentation of this work benefited from informal reviews by O. Bachmann and D. Rumble. Discussions with P. Ulmer, X. Zhong, J.A. Padron Navarta, D. Miron, D. Sverjensky, J. Eiler and J. Cohen were helpful. This research was supported by an ETH fellowship ETH/CoFUND FeI-06 13-2 (M.E.G.). Partial support from Carnegie and Society in Science/Branco-Weiss fellowships (M.E.G.), Swiss National Science Foundation Grant 200021_146872 (J.A.D.C.), Deep Carbon Observatory and National Science Foundation grant EAR 1347987 (C.E.M.) are also acknowledged.

Author Contributions M.E.G. conceived the project, developed the computational tools used and performed the calculations. J.A.D.C. developed the PerpleX software used for phase equilibria computations. M.E.G., J.A.D.C. and C.E.M. analysed the data and wrote the paper.

Author Information Reprints and permissions information is available at www.nature.com/reprints. The authors declare no competing financial interests. Readers are welcome to comment on the online version of the paper. Correspondence and requests for materials should be addressed to M.E.G. (matthieu.galvez@erdw.ethz.ch or matthieu.galvez@gmail.com).

Reviewer Information *Nature* thanks D. Dolejs, K. Evans and H. Keppler for their contribution to the peer review of this work.

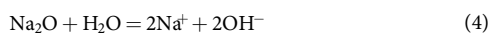
METHODS

Phase equilibria. Phase diagram sections have been computed by forward modeling (Gibbs energy minimization with PerpleX³⁴) using the 2002 revision of the Holland and Powell mineral database³⁵. Rock compositions are chosen to represent model pelite^{36,37}, K-free basalt³⁸ and peridotite (alkali-free lherzolite³⁹) systems (Extended Data Table 1) and maintain H₂O saturation ($a_{\text{H}_2\text{O}} = 1$ in pure H₂O systems, Figs 1, 2a, d) over the entire P - T field for fluid speciation calculation. The carbonated basalt is modified from the C-free composition to maintain fluid saturation (H₂O \approx 5.8 wt%) with \sim 2 wt% CO₂, consistent with average C content of the upper basaltic crust⁴⁰. Note that a harzburgite peridotite composition (Fe-Mg-Al-Si system) would dampen the ionic strength and ΔpH of the equilibrium fluid without significant change to their P - T behaviour. Component \mathcal{F} is modified from a representative crustal fluid composition from ref. 41. The solid solution models used include biotite (Bio)⁴², garnet (Grt)³⁵, chlorite (Chl)⁴³, staurolite (Sta)⁴⁴, white mica (Mus, Phe or Par)^{45,46}, K-feldspars (Kfs)⁴⁷, clinopyroxene (Cpx)⁴⁸, cordierite (Crd)⁴⁴, chloritoid (Ctd)⁴⁹, orthopyroxene (Opx)⁴⁸, plagioclase (Pl)⁵⁰, amphibole (Amp)⁵¹, carbonate (Do)³⁵, magnesite³⁵, antigorite (Atg)³⁹, olivine (O)³⁵ and an ideal solution model for talc (T). Minerals considered pure are quartz (Q), lawsonite (Law), kyanite (Ky), zoisite (Zo) and sillimanite (Sill). Additional mineral abbreviations: albite (Ab), jadeite (Jd), paragonite (Par), brucite (Brc). Two variants of the metasomatic model were considered: with (Fig. 3c, d) and without Na-phlogopite (aspidolite⁵²) for which thermochemical data are uncertain. In the absence of this phase, ΔpH (where $X_{\mathcal{F}} = 0.01$ – 0.43) increases by \sim 0.5 unit without change to the main features of the diagram. Wet melting curves for basalt and pelite are indicative, and drawn from experimental data in refs 53–55, carbonated-basalt melting curve is from experimental data in ref. 16.

P - T paths. Two model top-of-the-slab P - T paths represent cold (Central-Honshu⁵⁶ referred to as 'Honshu') and intermediate (Columbia-Ecuador⁵⁶ referred to as 'Columbia') thermal regimes. An indicative hot P - T path representative of Archaean subduction has been computed with a mantle potential temperature of $T = 1,650$ °C and parameters from the Cascadia subduction zone⁵⁶. We thank P. Van Keken for computing and providing the P - T coordinates of this geotherm. In combination, these paths are reasonable approximations for a broad range of possible geotherms likely to be realized in subduction zones from the Archaean to the Phanerozoic⁵⁷.

Solvent definition. Neutrally charged solvent species (for example, H₂O, CO₂, CH₄) are described by non-ideal molecular solution models. They are used to compute the phase diagram sections (Fig. 1) and the solvent dielectric constant (see below). Two distinct models are used for C-saturated C-O-H solvents⁵⁸ (graphitic pelite in Fig. 2b), and for binary H₂O-CO₂ solvents⁵⁹ (carbonated basalt in Fig. 2b). They define the solvents in which solute speciation is computed. This strategy differs from previous approaches^{60,61} in that C solubility predictions are consistent with independent constraints from both low- T congruent mineral dissolution (calcite⁶²) and high- T mixed-volatile carbonate-silicate incongruent dissolution experiments²⁵ over an extensive range of P , T and water activities. Our terminology differs in that congruent and incongruent carbonate dissolution at sub-solidus conditions are distinguished here, as opposed to dissolution versus decarbonation elsewhere^{61,63}.

Speciation calculation. At equilibrium the oxide chemical potentials are linked to the partial molar Gibbs energy of corresponding dissociated species through general hydrolysis equilibria such as:



This equation, and equivalent ones for all solutes considered (Extended Data Table 2) generates a set of equations of the form presented in Equation (1) (see main text). Together with water hydrolysis:



charge balance in the fluid $\sum_j Z_j m_j = 0$ (Z_j is the ionic charge, m_j the molality) and

an activity model for electrolytes, the equations governing fluid speciation are closed.

The chemical potentials of oxide components are obtained by differentiation of the extensive Gibbs energy of the system. It is assumed that the solutes do not affect the rock composition and mineralogy. This is a reasonable assumption in high- P subduction zone environments characterized by elevated rock/fluid ratio of interest here. The standard-state Gibbs energy of aqueous species is computed with the Helgeson–Kirkham–Flowers equation of state (EoS)^{20,64–68} using the Born model, extended here to mixed-volatile carbonic solvents²¹, adopting the convention $g_{\text{H}^+}^\ominus = 0$ (see main text). The thermochemical database for aqueous species and sources of those data are compiled in Extended Data Table 2. Consistency between

mineral and solute thermochemical database is judged adequate for the present purpose. Further discussions can be found in refs 21, 35, 69, 70.

Dissolved solutes that exert a dominant control on charge balance, ionic strength and computed pH, are Na⁺, OH[−] and HSiO₃[−] at all conditions for the pelite and basalt fluids, and Ca²⁺, CaOH⁺ and OH[−] (and AlO₂[−] along the hot geotherm) for the peridotite fluids. We estimate the precision on absolute ΔpH values is \pm 0.2 ΔpH (mainly due to uncertainty of thermodynamic data). In absence of experimental validations, the predictive accuracy is within 1 ΔpH unit. Relative variations and discontinuities are robust.

Fluid dielectric properties, standard state and activity model for solutes. The dielectric constant (static relative permittivity) of water is from refs 19, 20, 71 and 72, used in the Born dielectric continuum model of electrolyte solvation⁷³. Those of the mixed-volatile solvents are computed with a method developed in ref. 21. It uses the Landau–Lifschitz–Looyenga mixing scheme^{22,74,75} with volume fractions of solvent components computed with a reduced density method⁷⁶. Input solvent density at critical and target P , T conditions are derived from the molecular fluid EoS (see above).

The energetics of the solutes in going from pure H₂O to a mixed-volatile solvent characterized by ϵ_{mix} , is incorporated to the standard-state Gibbs energy of the solute^{77,78}, that is, it affects the equilibrium constants of homogeneous oxide-solutes equilibria in solution. Solute standard-state is unit activity of 1 mol of solute in 1 kg of solvent, referenced to infinite dilution. Aqueous species molal concentration is given in mol per kg of solvent.

Non-ideality for electrolytes follows the Davies extension of the Debye–Hückel law in its original 1938 formulation⁷⁹. The ionic strength of the solution (I) is linked to the activity coefficient (γ_j) of the j th anion or cation by $\log \gamma_j = \frac{-AZ_j^2 I^{1/2}}{(1 + I^{1/2})} + 0.2Z_j^2 I$,

where $I = \frac{1}{2} \sum_j Z_j^2 m_j$, $A = 1.82483 \times 10^6 \rho_{\text{mix}}^{1/2} (\epsilon_{\text{mix}} T)^{-3/2}$, m_j refers to the mola-

lity of the ion, A is the Debye–Hückel parameter, and ρ_{mix} and ϵ_{mix} are respectively the density and dielectric constant of the solvent. Using a coefficient $C = 0.3$ (ref. 79) instead of $C = 0.2$ (ref. 80) in the empirical term $CZ_j^2 I$ introduced no noticeable change to the results presented. The activity coefficient for neutral solutes is 1. The concentration of chlorine (for example, Fig. 2c, f) is set by fixing the total chlorine ($\sum \text{Cl}$) content of the fluid (Cl[−], HCl, NaCl \pm KCl solutes) to $\sum \text{Cl} = 1$ molal. Further technical details can be found in ref. 21.

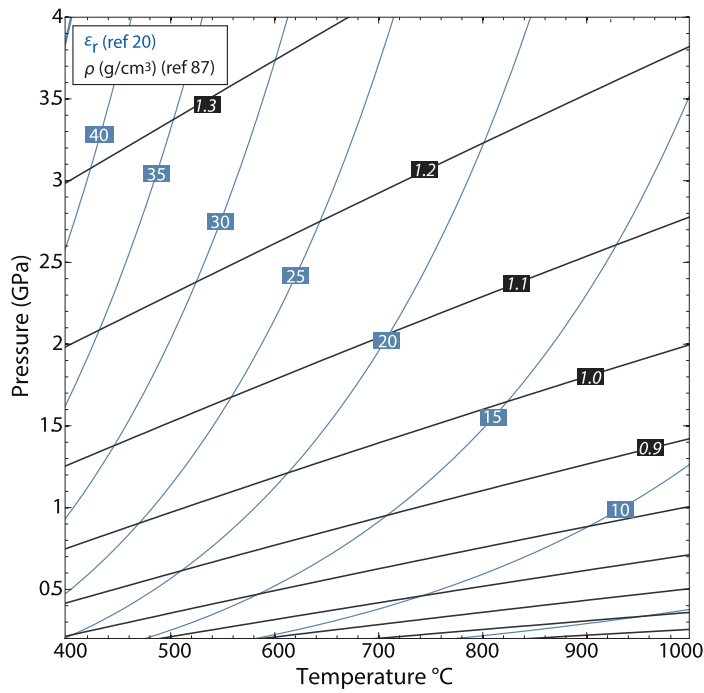
C flux estimates along cold and hot paths. Although subduction zone elemental budgets are sensitive to lithosphere hydration, overall length of subduction trenches, composition of subducting materials, geotherms and thus fluid fluxes, provisional estimates can be derived combining element solubility (this work) with fore-arc (<100 km depth, ref 81) and sub-arc (100 to 150 km depth) H₂O flux computed from ref. 81, assuming 2% H₂O in the upper 4 km of the oceanic mantle (Extended Data Table 3). Focusing on carbon, assuming a total length of 3.85×10^7 m of subduction trenches, a cold subduction (model based on the central Honshu system) results in a global annual sub-solidus C flux, combining forearc and sub-arc fluxes, of $\phi_{\text{C}} = 10 \pm 7$ Mt yr^{−1}. This corresponds to a net equivalent O flux beyond subarc depth of about 105 ± 50 Mt yr^{−1} (or redox budget flux (see ref 6) of 14 ± 7 Tmol yr^{−1} assuming C⁰ (elemental C) is the reference C oxidation state in the deep upper mantle), assuming a subduction C input of 40 – 66 Mt yr^{−1} (refs 61). Conversely, along the hot geotherm (Figs 1, 3b), the forearc flux alone is $\phi_{\text{C}} = 40 \pm 7$ Mt yr^{−1} that is within uncertainty of present-day subduction C input in ref. 61. This budget contrasts with cold regimes where up to 85% of the C input is retained in slabs, in agreement with conclusions from refs 82–85, and in partial contrast with challenging views⁶¹. Hot and intermediate paths (Columbia, Fig. 1a) typical of the Precambrian and rare modern settings are the only scenarios where substantial, possibly quantitative, forearc decarbonation may occur. In the latter intermediate scenario, quantitative C loss may occur, yet not by sub-solidus dissolution, but by carbonate melting^{16,83,86}. Slabs retaining \sim 40% of their initial C budget would cross the carbonated-basalt melting curve at sub-arc depth (Fig. 1a, see refs 16, 83, 86). Note that this temporal trend is consistent with previous interpretation of kimberlite–diamond isotopic signatures reflecting little recycled components in the mantle⁶¹. The latter isotopic signatures may record C recycling under dominantly hot Archaean and proterozoic subduction thermal regimes, and may not be representative of Phanerozoic and present-day subduction zones.

34. Connolly, J. A. D. Multivariable phase diagrams; an algorithm based on generalized thermodynamics. *Am. J. Sci.* **290**, 666–718 (1990).

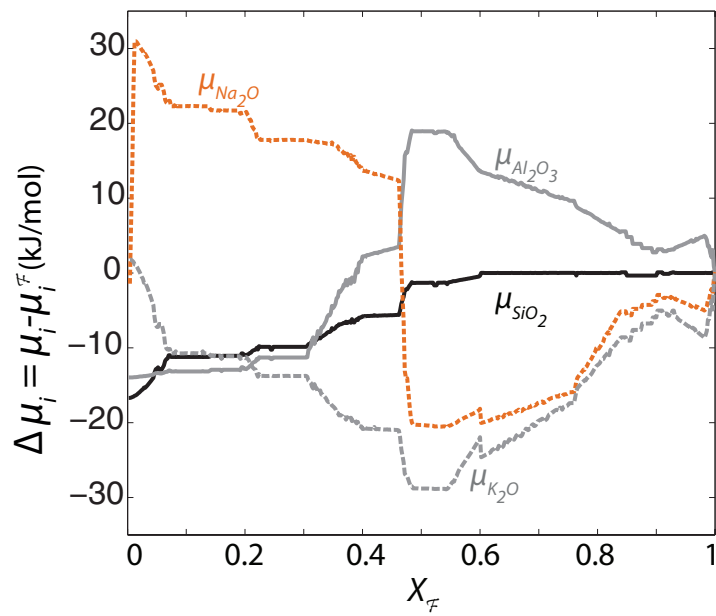
35. Holland, T. & Powell, R. An internally consistent thermodynamic data set for phases of petrological interest. *J. Metamorph. Geol.* **16**, 309–343 (1998).

36. Caddick, M. J. & Thompson, A. B. Quantifying the tectono-metamorphic evolution of pelitic rocks from a wide range of tectonic settings: mineral compositions in equilibrium. *Contrib. Mineral. Petrol.* **156**, 177–195 (2008).

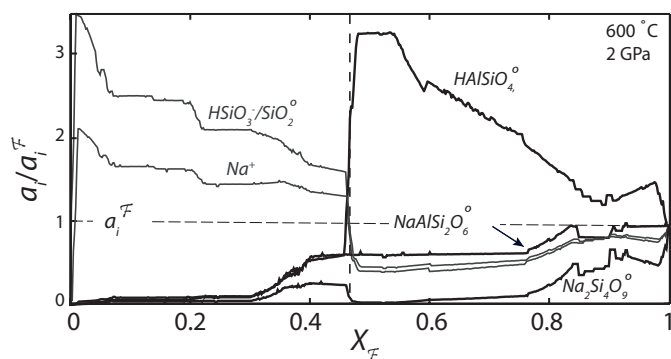
37. Shaw, D. M. Geochemistry of pelitic rocks. Part III: Major elements and general geochemistry. *Geol. Soc. Am. Bull.* **67**, 919–934 (1956).
38. Pearce, J. A. Statistical analysis of major element patterns in basalts. *J. Petrol.* **17**, 15–43 (1976).
39. Padrón-Navarta, J. A. *et al.* Tschermak's substitution in antigorite and consequences for phase relations and water liberation in high-grade serpentinites. *Lithos* **178**, 186–196 (2013).
40. Alt, J. C. & Teagle, D. A. H. The uptake of carbon during alteration of ocean crust. *Geochim. Cosmochim. Acta* **63**, 1527–1535 (1999).
41. Hermann, J., Zheng, Y.-F. & Rubatto, D. Deep fluids in subducted continental crust. *Elements* **9**, 281–287 (2013).
42. Tajčmanová, L., Connolly, J. A. D. & Cesare, B. A thermodynamic model for titanium and ferric iron solution in biotite. *J. Metamorph. Geol.* **27**, 153–165 (2009).
43. Holland, T., Baker, J. & Powell, R. Mixing properties and activity-composition and relationships of chlorites in the system MgO-FeO-Al₂O₃-SiO₂-H₂O. *Eur. J. Mineral.* **10**, 395–406 (1998).
44. Mahar, E. M., Baker, J. M., Powell, R., Holland, T. J. B. & Howell, N. The effect of Mn on mineral stability in metapelites. *J. Metamorph. Geol.* **15**, 223–238 (1997).
45. Coggon, R. & Holland, T. J. B. Mixing properties of phengitic micas and revised garnet-phengite thermobarometers. *J. Metamorph. Geol.* **20**, 683–696 (2002).
46. Auzanneau, E., Schmidt, M. W., Vielzeuf, D. & Connolly, J. D. Titanium in phengite: a geobarometer for high temperature eclogites. *Contrib. Mineral. Petrol.* **159**, 1–24 (2010).
47. Waldbaum, D. R. & Thompson, J. B. Mixing properties of sanidine crystalline solutions. 2. Calculations based on volume data. *Am. Mineral.* **53**, 2000–2017 (1968).
48. Holland, T. & Powell, R. Thermodynamics of order-disorder in minerals: II. Symmetric formalism applied to solid solutions. *Am. Mineral.* **81**, 1425–1437 (1996).
49. White, R. W., Powell, R., Holland, T. J. B. & Worley, B. A. The effect of TiO₂ and Fe₂O₃ on metapelitic assemblages at greenschist and amphibolite facies conditions: mineral equilibria calculations in the system K₂O-FeO-MgO-Al₂O₃-SiO₂-H₂O-TiO₂-Fe₂O₃. *J. Metamorph. Geol.* **18**, 497–511 (2000).
50. Newton, R. C., Charlu, T. V. & Kleppa, O. J. Thermochemistry of the high structural state plagioclases. *Geochim. Cosmochim. Acta* **44**, 933–941 (1980).
51. Dale, J., Powell, R., White, R., Elmer, F. & Holland, T. A thermodynamic model for Ca-Na clinopyroxenes in Na₂O-CaO-FeO-MgO-Al₂O₃-SiO₂-H₂O for petrological calculations. *J. Metamorph. Geol.* **23**, 771–791 (2005).
52. Pirard, C. & Hermann, J. Experimentally determined stability of alkali amphibole in metasomatised dunite at sub-arc pressures. *Contrib. Mineral. Petrol.* **169**, 1–26 (2015).
53. Hack, A. C., Thompson, A. B. & Aerts, M. Phase relations involving hydrous silicate melts, aqueous fluids, and minerals. *Rev. Mineral. Geochem.* **65**, 129–185 (2007).
54. Kessel, R., Ulmer, P., Pettke, T., Schmidt, M. W. & Thompson, A. B. The water-basalt system at 4 to 6 GPa: phase relations and second critical endpoint in a K-free eclogite at 700 to 1400°C. *Earth Planet. Sci. Lett.* **237**, 873–892 (2005).
55. Schmidt, M. W. & Poli, S. Experimentally based water budgets for dehydrating slabs and consequences for arc magma generation. *Earth Planet. Sci. Lett.* **163**, 361–379 (1998).
56. Syracuse, E. M., van Keken, P. E. & Abers, G. A. The global range of subduction zone thermal models. *Phys. Earth Planet. Inter.* **183**, 73–90 (2010).
57. Penniston-Dorland, S. C., Kohn, M. J. & Manning, C. E. The global range of subduction zone thermal structures from exhumed blueschists and eclogites: rocks are hotter than models. *Earth Planet. Sci. Lett.* **428**, 243–254 (2015).
58. Connolly, J. A. D. & Cesare, B. C-O-H-S fluid composition and oxygen fugacity in graphitic metapelites. *J. Metamorph. Geol.* **11**, 379–388 (1993).
59. Holland, T. & Powell, R. Activity-composition relations for phases in petrological calculations: an asymmetric multicomponent formulation. *Contrib. Mineral. Petrol.* **145**, 492–501 (2003).
60. Kerrick, D. M. & Connolly, J. A. D. Metamorphic devolatilization of subducted marine sediments and the transport of volatiles into the Earth's mantle. *Nature* **411**, 293–296 (2001).
61. Kelemen, P. B. & Manning, C. E. Reevaluating carbon fluxes in subduction zones, what goes down, mostly comes up. *Proc. Natl Acad. Sci. USA* **112**, E3997–E4006 (2015).
62. Caciagli, N. C. & Manning, C. E. The solubility of calcite in water at 6–16 kbar and 500–800°C. *Contrib. Mineral. Petrol.* **146**, 275–285 (2003).
63. Frezzotti, M. L., Selverstone, J., Sharp, Z. D. & Compagnoni, R. Carbonate dissolution during subduction revealed by diamond-bearing rocks from the Alps. *Nat. Geosci.* **4**, 703–706 (2011).
64. Helgeson, H. C., Kirkham, D. H. & Flowers, G. C. Theoretical prediction of the thermodynamic behavior of aqueous electrolytes by high pressures and temperatures; IV. Calculation of activity coefficients, osmotic coefficients, and apparent molal and standard and relative partial molal properties to 600 degrees C and 5 kb. *Am. J. Sci.* **281**, 1249–1516 (1981).
65. Tanger, J. C. & Helgeson, H. C. Calculation of the thermodynamic and transport properties of aqueous species at high pressures and temperatures; revised equations of state for the standard partial molal properties of ions and electrolytes. *Am. J. Sci.* **288**, 19–98 (1988).
66. Helgeson, H. C. & Kirkham, D. H. Theoretical prediction of the thermodynamic behavior of aqueous electrolytes at high pressures and temperatures; II. Debye-Huckel parameters for activity coefficients and relative partial molal properties. *Am. J. Sci.* **274**, 1199–1261 (1974).
67. Helgeson, H. C. & Kirkham, D. H. Theoretical prediction of the thermodynamic behavior of aqueous electrolytes at high pressures and temperatures; I. Summary of the thermodynamic/electrostatic properties of the solvent. *Am. J. Sci.* **274**, 1089–1198 (1974).
68. Helgeson, H. C. & Kirkham, D. H. Theoretical prediction of the thermodynamic properties of aqueous electrolytes at high pressures and temperatures. III. Equation of state for aqueous species at infinite dilution. *Am. J. Sci.* **276**, 97–240 (1976).
69. Sverjensky, D. A., Hemley, J. & d'Angelo, W. Thermodynamic assessment of hydrothermal alkali feldspar-mica-aluminosilicate equilibria. *Geochim. Cosmochim. Acta* **55**, 989–1004 (1991).
70. Miron, G. D., Wagner, T., Kulik, D. A. & Heinrich, C. A. Internally consistent thermodynamic data for aqueous species in the system Na-K-Al-Si-O-H-Cl. *Geochim. Cosmochim. Acta* **187**, 41–78 (2016).
71. Fernández, D. P., Mulev, Y., Goodwin, A. & Sengers, J. L. A database for the static dielectric constant of water and steam. *J. Phys. Chem. Ref. Data* **24**, 33–70 (1995).
72. Fernández, D., Goodwin, A., Lemmon, E. W., Sengers, J. L. & Williams, R. A formulation for the static permittivity of water and steam at temperatures from 238 K to 873 K at pressures up to 1200 MPa, including derivatives and Debye-Hückel coefficients. *J. Phys. Chem. Ref. Data* **26**, 1125–1166 (1997).
73. Bockris, J. O. M. & Reddy, A. K. N. *Modern Electrochemistry: An Introduction to an Interdisciplinary Area* Vol. 2 (Springer, 1973).
74. Landau, L. D. & Lifshitz, M. *Electrodynamics of Continuous Media* (Pergamon, 1960).
75. Looyenga, H. Dielectric constants of heterogeneous mixtures. *Physica* **31**, 401–406 (1965).
76. Harvey, A. H. & Prausnitz, J. M. Dielectric constants of fluid mixtures over a wide range of temperature and density. *J. Solution Chem.* **16**, 857–869 (1987).
77. Walther, J. V. Ionic association in H₂O-CO₂ fluids at mid-crustal conditions. *J. Metamorph. Geol.* **10**, 789–797 (1992).
78. Akiniev, N. & Zotov, A. Thermodynamic description of equilibria in mixed fluids (H₂O-non-polar gas) over a wide range of temperature (25–700°C) and pressure (1–5000 bars). *Geochim. Cosmochim. Acta* **63**, 2025–2041 (1999).
79. Davies, C. W. *Ion Association* (Butterworths, 1962).
80. Davies, C. W. The extent of dissociation of salts in water. Part VIII. An equation for the mean ionic activity coefficient of an electrolyte in water, and a revision of the dissociation constants of some sulphates. *J. Chem. Soc.* 2093–2098 (1938).
81. van Keken, P. E., Hacker, B. R., Syracuse, E. M. & Abers, G. A. Subduction factory: 4. Depth-dependent flux of H₂O from subducting slabs worldwide. *J. Geophys. Res. Solid Earth* **116**, B01401 (2011).
82. Dasgupta, R. & Hirschmann, M. M. The deep carbon cycle and melting in Earth's interior. *Earth Planet. Sci. Lett.* **298**, 1–13 (2010).
83. Thomson, A. R., Walter, M. J., Kohn, S. C. & Brooker, R. A. Slab melting as a barrier to deep carbon subduction. *Nature* **529**, 76–79 (2016).
84. Connolly, J. A. D. Computation of phase equilibria by linear programming: a tool for geodynamic modeling and its application to subduction zone decarbonation. *Earth Planet. Sci. Lett.* **236**, 524–541 (2005).
85. Gorman, P. J., Kerrick, D. M. & Connolly, J. A. D. Modeling open system metamorphic decarbonation of subducting slabs. *Geochem. Geophys. Geosyst.* **7**, Q04007 (2006).
86. Skora, S. *et al.* Hydrous phase relations and trace element partitioning behaviour in calcareous sediments at subduction-zone conditions. *J. Petrol.* **56**, 953–980 (2015).
87. Zhang, Z. & Duan, Z. Prediction of the PVT properties of water over wide range of temperatures and pressures from molecular dynamics simulation. *Phys. Earth Planet. Inter.* **149**, 335–354 (2005).
88. Pokrovskii, V. A. & Helgeson, H. C. Thermodynamic properties of aqueous species and the solubilities of minerals at high pressures and temperatures; the system Al₂O₃-H₂O-NaCl. *Am. J. Sci.* **295**, 1255–1342 (1995).
89. Pokrovskii, V. A. & Helgeson, H. C. Thermodynamic properties of aqueous species and the solubilities of minerals at high pressures and temperatures: the system Al₂O₃-H₂O-KOH. *Chem. Geol.* **137**, 221–242 (1997).
90. Sverjensky, D. A., Shock, E. L. & Helgeson, H. C. Prediction of the thermodynamic properties of aqueous metal complexes to 1000°C and 5 kb. *Geochim. Cosmochim. Acta* **61**, 1359–1412 (1997).
91. Xie, Z. & Walther, J. V. Wollastonite+ quartz solubility in supercritical NaCl aqueous solutions. *Am. J. Sci.* **293**, 235–255 (1993).
92. Miron, G. D. *Internally Consistent Thermodynamic Database for Fluid-Rock Interaction: Tools, Methods and Optimization*. Dissertation no. 23242, ETH-Zurich (2016).



Extended Data Figure 1 | Properties of water at geological conditions.
 The relative permittivity²⁰ (ϵ_r) and density⁸⁷ (ρ) of pure water as functions of pressure and temperature. Adapted from ref. 21.



Extended Data Figure 2 | Oxide chemical potential across a peridotite–crust interface. Shown are profiles of oxide chemical potentials (μ) in the metasomatic model (Fig. 3c, d) relative to that for component \mathcal{F} ($\mu_i^{\mathcal{F}}$) at 600 °C and 2 GPa.



Extended Data Figure 3 | Relative activity of selected neutral species across a serpentinite-crust interface. Shown are relative activities

$$\left(\frac{a_i}{a_i^F}\right)_{P,T}^{\text{fluid}} = \exp\left[\frac{1}{RT}\left(\mu_i - \mu_i^F\right)_{P,T}\right]^{\text{rock}}$$

of neutral polynuclear clusters HAlSiO_4^0 , $\text{NaAlSi}_2\text{O}_6^0$ and $\text{Na}_2\text{Si}_4\text{O}_9^0$, as well as Na^+ and $\text{HSiO}_3^-/\text{SiO}_2^0$, in the fluid, at 600 °C and 2 GPa (see Fig. 3c, d).

Extended Data Table 1 | Rock compositions used for phase equilibria computations

	SiO ₂	Al ₂ O ₃	Na ₂ O	K ₂ O	MgO	CaO	FeO	H ₂ O	CO ₂
Pelite ⁱ	65.6	18.17	1.89	3.87	2.87	1.19	6.37	sat. ^{vi}	
Basalt ⁱⁱ	51.6	16	2.6	0	7.7	11.3	10.8	sat.	
Basalt+C ⁱⁱⁱ	47.5	14.7	2.4	0	7.1	10.4	9.9	5.85	2.02
Peridotite ^{iv}	46.11	4.52	0	0	39.05	3.26	7.04	sat.	
Fcomponent ^v	70.11	12.74	5.16	2.61	2.24	3.11	3.99	sat.	

ⁱComposition from ref. 36, the C-saturated pelite with fluid atomic ratio O/H=0.5 has a similar oxide composition.

ⁱⁱModified from ref. 38.

ⁱⁱⁱModified from ref. 38.

^{iv}Composition from ref. 39.

^vComposition from ref. 41.

^{vi}sat., saturated.

Extended Data Table 2 | Thermodynamic data source for solutes used in this study

Inorganic species				C species			Cl species		
SiO_2^0	<i>a</i>	KOH^0	<i>d</i>	MgSiO_3^0	<i>h</i>	HCO_3^-	<i>a</i>	HCl^0	<i>a</i>
Si_2O_4^0	<i>a</i>	K^+	<i>a</i>	Fe^{2+}	<i>a</i>	CO_3^{2-}	<i>a</i>	NaCl^0	<i>a</i>
HSiO_3^-	<i>b</i>	KAlO_2^0	<i>e</i>	OH^-	<i>a</i>	HCOO^-	<i>a</i>	KCl^0	<i>a</i>
HAlO_2^0	<i>a</i>	Ca(OH)^+	<i>a</i>			NaCO_3^-	<i>a</i>	Cl^-	<i>a</i>
AlO_2^-	<i>a</i>	Ca^{2+}	<i>a</i>			NaHCO_3^0	<i>a</i>		
Na(OH)^0	<i>a</i>	CaHSiO_3^+	<i>f</i>			CaHCO_3^+	<i>a</i>		
Na^+	<i>a</i>	CaSiO_3^0	<i>g</i>			MgHCO_3^+	<i>a</i>		
NaAlO_2^0	<i>c</i>	Mg(OH)^+	<i>a</i>			MgCO_3^0	<i>a</i>		
NaHSiO_3^0	<i>a</i>	MgHSiO_3^+	<i>a</i>			CaCO_3^0	<i>a</i>		

^aData as reported in the Deep Earth Water (DEW) database, (ref. 20).

^bData as reported in the DEW database, (ref. 20).

^cFrom ref. 88.

^dAs reported in ref. 20.

^eFrom ref. 89.

^fModified from ref. 90 to obtain a_1 parameter (HKF volumetric coefficient) consistent with the sum of the revised a_1 of Ca^{2+} and HSiO_3^- .

^gEstimates from data at 25 °C for CaSiO_3^0 from cement phase solubility, and wollastonite solubility from ref. 91 (compare ref. 92).

^hAssumed to have the same logK of formation as CaSiO_3^0 , from ref. 92.

Extended Data Table 3 | Estimates of global annual C fluxes

	H ₂ O flux ^a (Mt/yr)		C concentration (mol/kg H ₂ O)		C flux (Mt/yr)		
	forearc	subarc ^b	forearc	subarc	forearc	subarc	total
Central Honshu	277	177	0.3–3 ^c	1–3 ^d	5 ± 4	4 ± 2	10 ± 7
Columbia-Ecuador	420	454	1–10	7–10 ^e	28 ± 23	46 ± 8 [*]	74 ± 31 [*]
Mexico ('Archean') ^f	474	235	4–10 ^{e,*}	7–10 ^e	40 ± 17 [*]	24 ± 4 [*]	64 ± 21 [*]
Global average	331	130	0.3–6 [*]	3–6 [*]	13 ± 11 [*]	7 ± 2 [*]	20 ± 14 [*]

Shown are estimates of global annual C fluxes derived from C solubility data (this study) and H₂O fluxes from subducting slabs (ref. 81).

^aThe global annual H₂O flux for each subduction locality is obtained by multiplication of the annual H₂O flux per metre of trench by the entire length of the present subduction trenches, that is, 38.5×10^6 m (ref. 81). The global average is obtained from ref. 81. C concentrations for the global (present-day) average are indicative, intermediate between the Honshu and Columbia endmembers scenario.

^bSubarc H₂O flux are released from slabs between 100 and 150 km depth.

^cThe value of 0.3 mol C per kg H₂O is at ~500 °C (Fig. 3a), and 3 mol C per kg H₂O is a conservative estimate at ~650–700 °C and ~3 GPa (Fig. 3a).

^dThe concentration range 1–3 mol C per kg H₂O accounts for the decrease in C solubility with *P* increase along the high-T section of the P-T path.

^eThe value of 4 mol C per kg H₂O is at 600 °C, Fig. 3b, increasing to ~10 mol C per kg H₂O at ~700–750 °C.

^fThe H₂O fluxes for the model Archean scenario are those computed from the Mexico geotherm (ref. 81).

^{*}The solidus may be crossed along the path. Rock partial melting may significantly affect the values reported.